A multi-objective optimization to characterize the diffusion of nanocavities in tungsten

Andrée de Backer, Abdelkader Souidi, Etienne A. Hodille, Emmanuel Autissier, Cécile Genevois, Farah Haddad, Antonin Della Noce, Christophe Domain, Charlotte Becquart, Marie France Barthe

Computational Materials Science 248 (2025) 113570

Contents lists available at ScienceDirect

Computational Materials Science

journal homepage: www.elsevier.com/locate/commatsci

Full length article

A multi-objective optimization to characterize the diffusion of nanocavities in tungsten

Andrée De Backer [a,b,c,*], Abdelkader Souidi [d], Etienne A. Hodille [e], Emmanuel Autissier [f], Cécile Genevois [f], Farah Haddad [f], Antonin Della Noce [g], Christophe Domain [h,b], Charlotte S. Becquart [a,b], Marie France Barthe [f]

[a] Univ. Lille, CNRS, INRAE, Centrale Lille, UMR 8207 - UMET - Unité Matériaux et Transformations, F-59000 Lille, France
[b] EM2VM, Joint laboratory Study and Modelling of the Microstructure for Ageing of Materials, France
[c] Aix Marseille Univ, CNRS, PIIM, F-13013 Marseille, France
[d] Université Dr. Tahar Moulay de Saida, Faculté des Sciences, Département de physique, En-nasr BP138, Saida 20000, Algeria
[e] CEA, IRFM, F-13108, Saint Paul lez Durance, France
[f] CNRS-CEMHTI, 3A rue de la Férollerie, F-45071, ORLEANS cedex 2, France
[g] Institut de Cancérologie Gustave Roussy, IGR, Unité INSERM 981, F-94805 Villejuif, France
[h] EDF-R&D, Département Matériaux et Mécanique des Composants, Les Renardières, F-77250, Moret sur Loing, France

ARTICLE INFO

Dataset link: https://data.mendeley.com/my-data/

Keywords:
Multi-objective optimization
Pareto front
OKMC
Irradiation damage
Defect microstructure
Nanocavity diffusion

ABSTRACT

We characterize the diffusion properties of nanocavities and their uncertainties by designing a multi-objective optimization approach. In this work, the nanocavity diffusion on the 0.3–4 nm size range is the input of a multi-scale simulation that is adjusted to reproduce experimental results of a systematic study of nanocavity growth with temperature up to 1773 K. Under irradiation, in the material microstructure, the damage evolution results from a complicated interplay of the defects and their clusters (formed from the vacancies and self-interstitials created) which diffuse, recombine and grow. The simulation of the whole experiment, based on an Object Kinetic Monte Carlo algorithm, can take several hours per condition which is a strong limitation for the optimization scheme. We describe the method that succeeds for our problem. Starting from a rough and random sampling of the space of parameters, we then consider that each simulation is one point of the hypersurface in the high dimensional space formed by the optimized parameters and objectives. We iteratively improve the characterization of this hypersurface where the objectives are optimum thanks to a systematic search of patterns formed by points on the coordinate planes. The non-dominated solutions, i.e. the equally good solutions, also named the Pareto front, are finally characterized. They draw two "valleys" in the subspace of parameters, delimiting the uncertainties on the searched diffusion properties, which cannot be reduced with the experimental data and the model in their current form.

1. Introduction

Materials are exposed to severe damaging conditions in nuclear energy production devices: the fission reactors and the fusion tokamaks (as ITER). The nuclear reactions produce neutrons which penetrate the facing materials, creating transmutation and microstructure defects (vacancies and self interstitial atoms (SIA)). The consequence is a complex damage evolution and a possible material degradation, due to the diffusion, recombination and agglomeration of these defects. In fusion tokamaks, in particular, the formation of nanocavities increases the retention of tritium [1] and modifies the mechanical properties [2]. To guarantee the safety of the reactors, dedicated experimental campaigns and multiscale modeling projects have been performed for decades to understand and model the evolution of microstructures under these conditions. Despite the amount of research already done on the subject, few data exist on the diffusion properties of the nanocavities. The main reasons are, on the one hand, that a significant part of the defects is not visible with typical means, i.e. microscopes, and on the other hand that realistic simulations of the damage evolution have to handle a large range of temperature-dependent processes. The diffusion, recombination and clustering of vacancy defects can be simulated by the Object Kinetic Monte Carlo (OKMC) approaches reviewed in [3,4], the diffusion equation models as in the early works [5,6] or, recently, in [7] where the mobility of all species is included or in [8,9] where it is not strictly included. Phase field approaches are also possible as

* Corresponding author at: Univ. Lille, CNRS, INRAE, Centrale Lille, UMR 8207 - UMET - Unité Matériaux et Transformations, F-59000 Lille, France.
E-mail address: charlotte.becquart@univ-lille.fr (C.S. Becquart).

https://doi.org/10.1016/j.commatsci.2024.113570
Received 20 October 2023; Received in revised form 25 November 2024; Accepted 25 November 2024
Available online 12 December 2024

in the review [10] where Li et al. show that in most of these models, only single vacancies are mobile because vacancy clusters are rarely considered. An exception is [11] where the migration of cavities is possible when they are large, via the surface diffusion mechanism. With the increase in computing power, the finite element scale is also accessible [12]. Regarding the theory of vacancy defect mobility, in the 1960s, the motion and coalescence of pores in metals have been intensively studied to understand the damage of materials in nuclear devices [13–15]. A surface diffusion model was developed, detailed by Goodhew in [14] referring to an earlier review of Nichols [13]. This pioneering work is limited to large defects and, to our knowledge, no data was published for tungsten. Interestingly, Trinkaus [15] investigated the effect of helium on the bubbles mobility. In 2017, three theoretical works based on atomic scale approaches in tungsten have been published. Mason et al. calculated the migration energies of small vacancy clusters with Density Functional Theory [16]. Castin et al. characterized the diffusion properties of vacancy clusters using a machine learning approach and empirical potentials [17]. D. Perez et al. investigated the diffusion properties of small vacancy-helium complexes with an accelerated molecular dynamics method [18]. In [19,20], in iron, the migration energy of vacancy clusters of similar sizes can vary significantly because of changes of the cluster symmetry. The atomic structure of nanovoids in tungsten is precisely the subject of a recent paper [21].

On the experimental side, nowadays, papers report on the improvement of the electron microscope performances and the development of automatic analysis, allowing accurate and efficient counting of small nanocavities [22,23].

In our paper, we propose to bridge the gap between the smallest vacancy clusters for which theoretical approaches are possible and the several nanometer size cavities for which the classical surface diffusion theory is valid but no data exists. We combine a series of new microscopy results detailed in [22], an Object Kinetic Monte Carlo (OKMC) model of the creation and interaction of defects and a multi-objective optimization approach. The preliminary results of the multi-objective optimization have been briefly introduced in the MaxEnt 2022 conference proceedings [24]. Several improvements of our multiscale model have been described in a separated paper [25]. Regarding the experiment, in short, tungsten samples are first irradiated, which creates interstitial defects and vacancy defects (some small nanocavities are at the limit of detection of the microscope). Then, the samples are successively annealed at increasing temperature and the large density of small nanocavities turns into rarer but larger nanocavities. For the simulations, the OKMC model mimics the whole experiment: the irradiation and the annealing stages. The diffusion properties are some of the input parameters. The nanocavity densities and sizes are the outputs of the simulation, as in the experiment. We show in [25] that their diffusion is necessary and dominant compared to dissociation. The complexity of the optimization comes from the large dimension of the inputs and outputs of the model and the strong non linearity of the interactions simulated. We will describe quantitatively some of its properties, but sensitivity analyses (i.e. the response of the model predictions to variations in the input data) can be found in [25].

The first section starts with a brief summary of the physical processes, the mathematical formulation of the multi-objective optimization, the description of the experimental data and the description of the numerical model. In the second section, we describe the high dimensional space made of the searched input parameters and the objectives and the hypersurface determined by the multi-objective optimization. We detail the search for the non-dominated solutions which characterize the Pareto front thanks to the projections in the space. The manuscript ends with the discussion and conclusion.

2. Physical processes and methods

2.1. Physical processes

Lets consider three stages: the collision cascade (the first 10 ps after the impact of an energetic particle), the irradiation (damage accumulation) and the annealing stage (temperature increase). The high energy ion collides with atoms and transfers its kinetic energy when it kicks them out of their position in the crystal lattice. This series of initial events triggers a chain of collision named the *displacement cascade* [26]. The number of defects reaches a maximum at the maximum expansion of the cascades (around 0.5 ps). The *cooling down* phase follows with the crystal recovery and the defect recombination or clustering. After a few ps, the remaining SIA and vacancy defects form the *primary damage*. They are isolated (point defects), in small clusters or form dislocation loops and nanocavities. Under irradiation, defects accumulate. Some diffuse and new recombinations or cluster growth can take place. During the annealing stage (i.e. a temperature increase), the diffusion of defects so far immobile can be activated, restarting the microstructure evolution.

We now define the main inputs and outputs of the numerical model, the pertinent results of the experiment and the multi-objective optimization problem. To avoid confusion, we first start to state that we will describe two variables related to temperatures: the *annealing* temperatures and the *diffusion* temperatures. The annealing temperatures, T_j, are real temperatures at which the samples are set to during the annealing stages. They are fixed inputs of the model. The diffusion temperatures, $theta_i$, are the temperatures at which the diffusion coefficients of nanocavity size classes reach a given non negligible value. It is inspired by the expected temperature of the peak during the thermal desorption spectrometry as used in [27,28] with the limits explained in [29]. They are material properties which have been introduced to simplify the optimization problem and ease the interpretation of the simulations. They will be the model inputs that vary during the optimization work but it is important to clarify that the OKMC model uses proper diffusion coefficients (related to these diffusion temperatures). Intuitively three cases can be imagined:

- The diffusion temperature of a nanocavity size class is much smaller than the annealing temperature. These nanocavities diffuse quickly and interact, hence they rapidly disappear. They are actually not likely to be present at all. The sensitivity of the simulation at this annealing temperature is likely to be weak for this diffusion temperature.
- The diffusion temperature of a nanocavity size class is much larger than the annealing temperature. The nanocavities do not diffuse. If one reduces this diffusion temperature, the nanocavities, if they are present, will be set into slow motion and slightly impact the simulation results.
- Between these extreme conditions, there is a range of values of diffusion temperatures, close to the annealing temperatures, where the sensitivity can be maximum. The conditions are that the nanocavities must be present and interact with the other elements of the microstructure, which, in principle, depends on all the other parameters.

2.2. Mathematical formulation

The optimization will search N (=30) diffusion temperatures on a discretization of the size (diameter) range of 0.3 to 4 nm nanocavities. The relation with the thermally activated diffusion coefficient is given in Section 2.4, and we consider here a simple increasing function,

$$\begin{array}{ll} \theta_1 & \text{for the min size} \\ \delta\theta_i & \text{temperature increase (in } \mathbb{R}_+) \\ \theta_n = \theta_{n-1} + \delta\theta_n & n = 2 : N. \end{array} \quad (1)$$

From the experiment, we expect the *mean* size and *total* densities of nanocavities,

$$(t_j, T_j, density_j, size_j)_{1\leq j\leq M} \tag{2}$$

where t_j, T_j are the time and annealing temperature. $M = 9$ is the number of observation stages, i.e. one irradiation and $M-1$ annealing stages. The relation between t_j and T_j is fixed because the observations are realized at the end of each stage. Thus one has only,

$$\begin{array}{l} T_1 \\ T_j = T_{j-1} + \delta T \quad \text{for } j = 2:M \text{ with } \delta T > 0 \end{array} \tag{3}$$

Note in Section 2.3 that the scattering of the experimental results is large and we thus adjusted a likelihood function called the *observed* total density and mean size,

$$\begin{array}{l} (density_{obs}(T_j), size_{obs}(T_j))|(density_{exp}, size_{exp}) \\ = \mathcal{P}_{likelihood}(T_j)|(density_{exp}, size_{exp}). \end{array} \tag{4}$$

The simulations mimic the experiment guessing the diffusion temperatures $\theta_{1:N}$ of (1). The outputs are the simulated total nanocavity densities and mean sizes for each annealing temperature:

$$(density_{sim}(T), size_{sim}(T)) \sim OKMC(T, \theta_{1:N}) \tag{5}$$

where $T \in [T_1 + (M-1)\delta T] \mapsto \mathrm{OKMC}(T, \theta_{1:N})$ is a stochastic process function of temperature and time as for the experiment.

We search the optimum diffusion temperatures $\theta_{1:N}$ which, ideally, minimize simultaneously M *density* and M *size* objectives. We define the error between *obs* and *sim* values, $\mathcal{D}(x_{obs}, x_{sim}) = \log(x_{obs}) - \log(x_{sim})$ and the error density probability, $E\left(\mathcal{D}(x_{obs}, x_{sim})\right) \propto \exp\left(-S|\mathcal{D}(x_{obs}, x_{sim})|\right)$, which is a particular case of the generalized normal distribution [30,31]. The choice of these expressions is not unique but reflects quantitatively the qualitative estimate when one human decides if the agreement between simulated and experimental data, is good or not. The $2M$ objectives are

$$\begin{array}{l} O_d^j(\theta_{1:N}) = \mathbb{E}\left\{E\left(\mathcal{D}(density_{obs}(T_j), density_{sim}(T_j))\right), \right. \\ \qquad \left. density_{sim}(T_j) \sim \mathrm{OKMC}(T_j, \theta_{1:N})\right\} \\ O_s^j(\theta_{1:N}) = \mathbb{E}\left\{E\left(\mathcal{D}(size_{obs}(T_j), size_{sim}(T_j))\right), \right. \\ \qquad \left. size_{sim}(T_j) \sim \mathrm{OKMC}(T_j, \theta_{1:N})\right\} \end{array} \tag{6}$$

for $j = 1:M$ where $\mathbb{E}$ represents a mean on OKMC simulations.

2.3. Experimental materials

First, one 33 nm thin spot is obtained with a twin-jet electropolisher in each cut and polished sample, which makes it locally transparent for the Transmission Electron Microscope (TEM).

Secondly, samples are irradiated with high energy ions (1.2 MeV W^+) at 773 K up to a fluence of 1.8×10^{16} m^{-2}. The level of damage is estimated to 0.02 dpa (displacement per atom), which means that, on average, 2% of the atoms have been involved in defects of the *primary damage*. As explained above, the surviving fraction of defects is much smaller.

Thirdly, samples are submitted to a succession of 1 h annealings at temperature plateaus of increasing setpoints: 873, 973, 1073, 1173, 1273, 1373, 1573 and 1773 K.

At the end of the irradiation and the annealing stages, the samples are cooled down and the microstructure are characterized by TEM. Fig. 1a shows two pictures in over- and under-focused conditions at the end of the irradiation stage. Nanocavities are defects whose contrast changes from black to white. Some of them are indicated by red circles revealing a large concentration of very small nanocavities.

The nanocavity total densities and mean sizes as a function of temperature are plotted in Fig. 2a. The visible scattering is partly due to the limited number of samples (micrographs per temperature) but mainly to variations of the local transparency and the different counting methods (human or automatic) [32,33]. On the same figure, lines represent the likelihood function introduced by Eqs. (4). The likelihood parameters are given in Appendix C. The lines delimit the value for which the objective will be respectively 0.1, 0.5 and 0.9 and capture

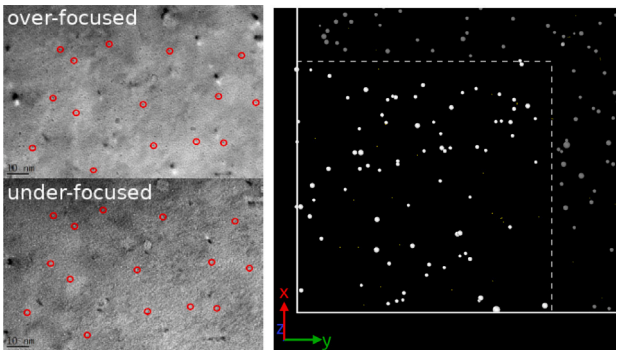

(a) (b)

Fig. 1. One 100 nm TEM micrograph of one irradiated sample in over and under-focused beam conditions. The cavities are defected where spots are black (resp. white) in the over (resp. under) focus condition. Some cavities are indicated by red circles and details of the manual and automatic methods of counting are given in [22]. (b) A zoomed picture of one OKMC box after irradiation. Only vacancy defects are shown. Yellow spheres, almost not visible in the picture, correspond to vacancy clusters smaller than the visibility limit (i.e. the minimum observable and quantifiable size in TEM pictures). The dashed lines indicate a distance of 100 nm from the box surface to help comparison with the experimental picture.

the point scattering. In Fig. 2, the error probability density is plotted as a function of the error and one sees that $S_d = 1$ for *density* and $S_s = 5$ for *size* strengthen the attach to *size* data.

When the temperature increases, the *density* decreases and *size* increases which can be explained by the progressive set into motion of the nanocavities by ascending size order. Most agglomerate and form larger nanocavities, in a process named *coalescence*, but some are eliminated at the sample surface or by recombination with SIA defects [22].

2.4. Simulation methods

With an OKMC approach, one easily implements many defect properties and many physical processes happening during irradiation, annealing and aging of materials. As indicated by its name, it is a stochastic model and the defects are considered as objects in a simulation box. They will be involved in processes characterized by as many parameters. The evolution is obtained by realizing random events following the Gillespie's algorithm [34]. Point defects (isolated and in clusters) are created throughout irradiation events. They are of opposite type: (+) for the SIA and (−) for the vacancy defects. They diffuse according to their properties. If two or more defects are found within pre-defined capture distances, the resulting defect type is the sum of the parent types. In principle, defect clusters can also dissociate but, as discussed in 4, this process in not activated in this work for vacancy defects.

The model inputs can be grouped in three categories given in Appendix A and detailed in [25]. We simply describe the parameters for the diffusion of vacancy defects. In real life, a significant displacement of the *center of mass* of a nanocavity results from many elementary processes [25] but, in the OKMC, it is simply simulated by random jumps of the object to nearest neighboring lattice sites. The jump probability is function of the defect size and temperature according to the Arrhenius formula,

$$f(s,T) = f(s)\exp\left(\frac{-E_m(s)}{k_B T}\right) \tag{7}$$

where s is the defect size, $f(s)$, the attempt frequency, $E_m(s)$, the migration energy and k_B, Boltzmann constant. Usually, experimental temperature ramps with various rate are necessary to determine simultaneously the model attempt frequency and the activation energy as

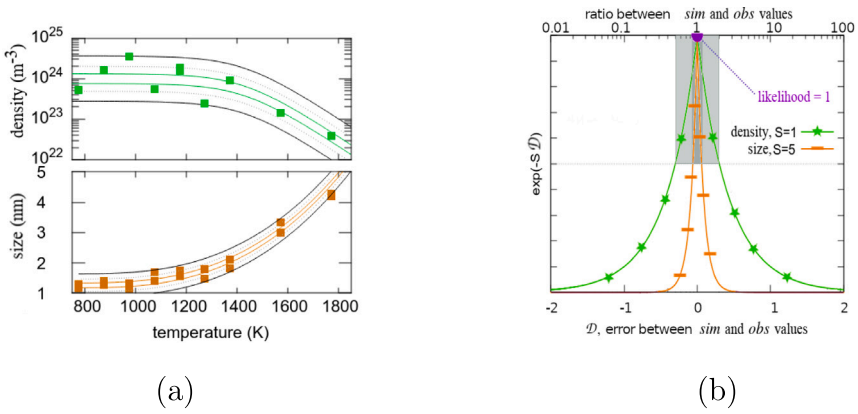

Fig. 2. (a) Experimental data: measured nanocavity total densities and mean sizes as a function of temperature, i.e. at the end of the irradiation stages and each of the 8 annealing stages. The lines indicate the values for which the objective will be equal to 0.1 0.5 and 0.9. (b) illustration of the error probability as a function of the error between observed and simulated results which describes how strongly the optimization should be attached to the likelihood (the top axis gives the ratio between *sim* and *obs*).

with the thermal desorption spectrometry or resistivity recovery, or at least a larger number of time versus temperature conditions than what we have. So we will assume N attempt frequencies, $f(s_i)$, justified in Appendix B and adjust the migration energies only. The relation between the migration energy and the diffusion temperature introduced in Eq. (1) is

$$E_m(s_i) = k_B \log(f(s_i))\,\theta_i. \tag{8}$$

where, here, $s_{1:N}$ is the list of N given size. The values for the sizes in between are interpolated. Notice that the diffusion coefficient, using the classical formula of [35], is

$$D = \frac{\alpha l^2}{2d} f(s,T) \tag{9}$$

with, in the case of bcc crystal, $l = \frac{\sqrt{3}}{2}a$, the jump length in our model, a the lattice parameter, $d = 3$, the dimension of the diffusion, $\alpha = 8$, the number of possible equivalent jumps on bcc lattice sites and $f(s,T)$, the jump rate given by Eq. (7).

3. Results

Preliminary tests of optimization show that weighted loss functions and the steepest descent approaches are particularly inefficient and the reasons are interesting and follow:

- the complex sensitivity of our model, schematized in Section 2.1, conditioned to the presence of nanocavities of the associated size class, not known a priori;
- the relation between the objectives from one temperature to the next, the quality of $O^j_{d,s}$ is conditioned to the one of $O^{j-1}_{d,s}$: in simple words, if a simulated result is far from the observed one at T_j, the chance to get it correct at $T_j + \delta T$ is low;
- an unexpected relationship between the *density* and *size* objectives: at each temperature stage, the optimization of *density*, O^j_d is obtained to the detriment of the *size* objective, O^j_s.

In [24], we proposed a simple relation between the diffusion temperature and the annealing temperature which simplified the optimization and permitted to find an approached solution. In this work, we describe how to represent the whole complexity of the data, search for patterns and how it improves the solution. One considers the high dimensional space formed by the N diffusion temperatures and the $2M$ objectives. The optimization problem becomes the parametric equation of one hypersurface. Each simulation is viewed as one point on the hypersurface with its coordinates being its N diffusion temperature and $2M$ objectives. Now, the optimization method aims to efficiently explore this space and concentrate the efforts on regions where some

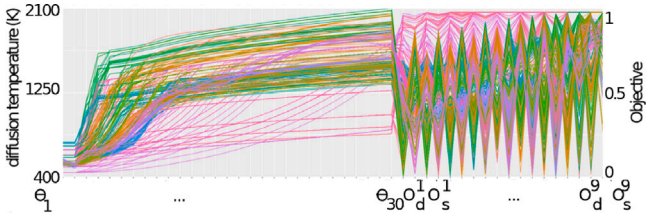

Fig. 3. The data accumulated during the optimization is a set of points with N coordinates in the parameter space and $2M$ coordinates in the objective space, shown here in a parallel coordinate plot. This is a graphical representation of points in a high dimensional space: each point is depicted as a line traversing a series of parallel axes, corresponding to, firstly, the N diffusion temperature, secondly, the $2M$ objectives, by temperature order. (The different colors help the reader to distinguish the different points of the data set).

of the objectives are small. It can be helped by any approaches to characterize the shape of this hypersurface and the search of patterns. The final set of points is represented in a parallel coordinate plot in Fig. 3. This is a graphical representation of points in a high dimensional space: each point is depicted as a line traversing a series of parallel axes, corresponding to, firstly, the N diffusion temperature, secondly, the $2M$ objectives, by temperature order. This arrangement is known to allow for the reveal of relationships or trends that might be obscured in raw data. Given that our method finally converged, the heterogeneous sampling of the subspace of the diffusion temperature might illustrate the efficiency of our exploration. Beside, the saw-tooth pattern in the objective subspace is due to the third point above: near explored regions, a good *size* objective is associated to a bad *density* objective and vice versa.

We now first look at the final set of points projected on M planes in the objective planes, secondly on $2M \times N$ planes corresponding to one of the objectives and one of the diffusion temperatures and finally in the parameter space.

3.1. Pareto front in the objective space

In Fig. 4 data are viewed in the $(O^s(1), O^d(1))$ plane, i.e. the objectives at the end of the irradiation. An additional information, the symbol color is the average of $\theta_{3:5}$. It corresponds to the diffusion temperature of the ~0.75 nm small clusters. The point size is the *size* at the end of the irradiation, $size_1$. One sees three branches named A, B and C joining in two locations a_d and a_s. a_d is the optimum for the *density* objective apparently for a diffusion temperature around 800 K. a_s is the *size* optimum obtained for a lower diffusion temperature around 650 K. Along branch A, one has different compromises of the *density* and *size* objective. An improvement of the *density* objective

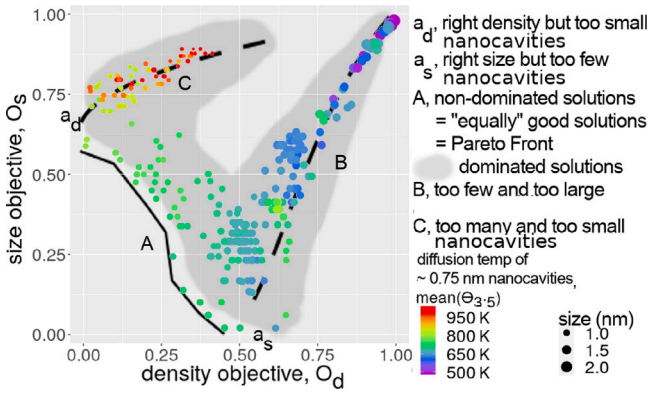

Fig. 4. The *size* objective as a function of the *density* objectives corresponding to the irradiation stage, i.e. O^1_d, O^1_s. The point colors correspond to the diffusion temperatures of the ∼0.75 nm nanocavities, mean($\theta_{3:5}$) and the point size corresponds to the mean size at the end of the irradiation, $size_1$. Two optimum points are labeled a_s (resp. a_d) and correspond to the best agreement with the *observed* density (resp. size) but to the detriment of the *size* objective and vice versa. Points along A are non-dominated solutions forming the Pareto Front. *B* and *C* branches are dominated solutions.

is accompanied by a deterioration of the *size* objective. This is the property of the Pareto optimal solutions.

This three branches pattern was globally observed on all planes of $O^d(T_j)$ and $O^s(T_j)$, i.e. for all annealing temperatures, as illustrated for 3 cases on Fig. 5. The branches are named A_j, B_j and C_j and limit points are a^j_d and a^j_s, where j is the index of the annealing temperature. The question is now how to determine the regions of the diffusion temperature subspace related to the a^j_d and a^j_s.

3.2. Projections on the crossed planes

There are $N \times 2M = 540$ planes each corresponding to one of the diffusion temperatures and one of the objective. Figs. 6, show three (θ_i, $O^j_{s,d}$), where pertinent patterns were detected. On the first one, points draw a V shape, indicating a strong sensitivity of θ_7 to the objective O^2_s. Thus it is a good projection to determine the optimum of θ_i for the *size* objective. The second plot is more a descending cloud of points and suggests a broad range of valid values for θ_7 to satisfy the *density* objective. In Fig. 6c, one sees a broad cloud of points. This plot is typical of the absence of strong correlation between the objective and the parameter. It can be explained by the fact that θ_{24} is the diffusion temperature of 3.25 nm nanocavities which are not supposed to be formed in none of the objectives at this temperature. The information that can be extracted from this plot is that small values of θ_{24} deteriorate the *size* objective.

The analysis of all planes highlight the main following observations:

- If a V shape is observed for one θ_i at T_j, the optimum value seems to be conserved at temperature higher $T_k, k > j$ even though the cloud of points can become more dispersed. This suggests that the Pareto Front can be described in the parameter space without ambiguity.
- blind spots are possible when the explored regions of the parameter space are too limited and mislead the interpretation.
- One property is caused by the physics of the simulated process: the indexes of θ_i where a V shape is observed progressively increases with the annealing temperature, hence the index j. The relation between i and j is different for *size* and *density*. The reason is that the microstructure evolution is a continuous set into motion of nanocavities by increasing size order.
- Because of the interdependence of the objectives, the good objectives at low temperature are the good view angle to efficiently explore the good objectives at high temperature.

3.3. Pareto front in the parameter space

We tried two simple methods to estimate automatically each $\Theta^j_{i_{d,s}}$ optimizing each $O^j_{d,s}$: by fitting a function in V on the points and by averaging the θ_i values for which the objectives are smaller than 0.25.

$2M\times$ lines $\Theta^j_{i_{d,s}}$ are drawn in the diffusion temperature space in Fig. 7. We observe two bundles of curves, corresponding to the *density* and the *size* objectives. Where the bundle of curves is narrow, the optimum of θ_i is estimated without ambiguity. This is the case for the small nanocavities because their diffusion impacts the beginning of the simulation hence the whole simulation. On the contrary, the bundle of curves broadens for the large sizes because only the last stages of the simulation (or none of them) are sensitive to this subset of parameters.

On Fig. 7, we indicate by squares the best $\Theta_{i_{d,s}}(j)$ among all $j = 1 : M$. Usually it is the one for which the standard deviation (represented by a bar) is the smallest. The color point indicates the corresponding T_j. We see that these temperatures increase with the nanocavity size, differently for *size* and *density* objective as explained above.

The Pareto front is now delimited in the parameter space. Additional simulations can be performed with parameters near the *density* and *size* optima. To give an idea of the problem size, around five hundred simulations are used for the results showed in this paper, which corresponds to 500–1000 h of computing time. Note however that OKMC computing times vary significantly with the input parameters.

3.4. Validation of the optimization method

A visual validation of the method is proposed using the parametric function described in Appendix F. In Fig. 8a, the diffusion temperatures as a function of the nanocavity sizes, obtained with expression (F.1) and data given in Table F.1 are drawn. The blue (resp. red) curves are for the *density* side of the Pareto front (resp. *size* side). In Fig. 8b and c, one sees the simulated *density* and *size* as a function of the annealing temperature superposed on the experimental likelihood and experimental points. The adequacy of the solutions is convincing: with the parameters of the *size* side of the Pareto front, the simulated *size* is correct but the simulated *density* significantly deviates and vice versa. The discrepancy due the Pareto front between *size* and *density* objectives is quite large and we showed in [24] that it is the main source of uncertainty on the diffusion temperature obtained in this work.

4. Discussion

One puzzling question raised by the optimization process is the origin of the Pareto front which underlines the fact that it is not possible to reproduce simultaneously the *density* and *size* objectives. A plausible explanation is a missing process in our model: a source of vacancy, probably at the interface between the bulk and oxide layer of the sample. This process is known, for example, in the corrosion mechanisms of zirconium alloys [36] but we explained in [24] that its implementation in our model would actually add more unknown parameters and not reduce the uncertainty on the nanocavity diffusion. Reversing the problem, we stress out that the multi-objective optimization quantified the impact of this missing process without having to model it.

The multi objective optimization brings out two elements of analysis:

- For each size class, drawing a vertical line from the lower Pareto front *size* side to the upper Pareto front *density* side can be seen as the **uncertainty** on the diffusion temperature, i.e. the limit of knowledge that can be extracted from our experimental data and our model in their current form.
- We can compare the source of uncertainties coming from the model and from the experimental data. At first glance, the experimental data seemed quite widely dispersed, especially on *density* data. Surprisingly, we found that the largest source of uncertainty comes from the model.

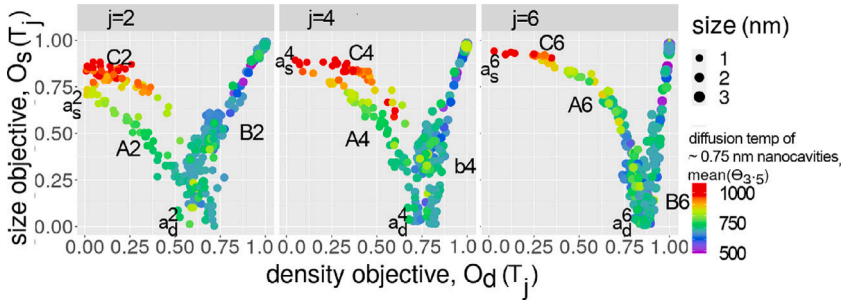

Fig. 5. Plots of the *density* objective as a function of the *size* objective of the components $j = 2, 4$ and 6 of the objective functions corresponding to $T_2 = 883$ K, $T_4 = 1073$ K and $T_6 = 1273$ K annealing stages. The point color corresponds to the diffusion temperature of the ~0.75 nm nanocavities. Points can be distinguished as non-dominated solutions forming the Pareto Front labeled A_j and dominated solution grouped in two branches named B_j and C_j.

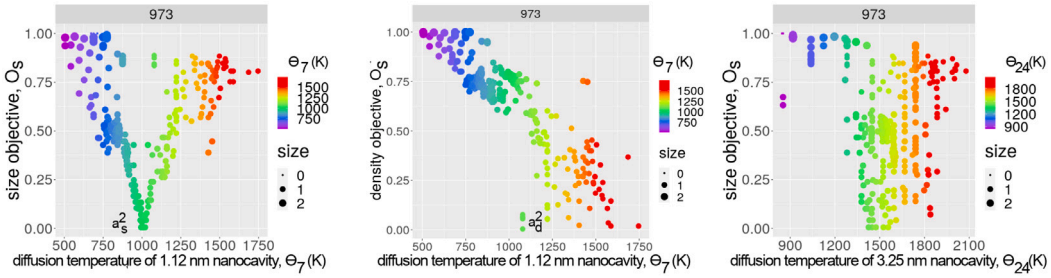

Fig. 6. Plots illustrating the optimum diffusion temperatures. For j = 2 ($T_2 = 973$ K), (a) the *size* objectives as a function of θ_7, the diffusion temperature of 1.12 nm nanocavities. (b) the *density* objectives as a function of θ_7, the diffusion temperature of 1.12 nm nanocavities. (c) the *size* objectives as a function of θ_{24}, the diffusion temperature of 3.25 nm nanocavities. The comparison of (a) and (b) shows that the optimal θ_7 is different for the *size* and *density* objectives as the values for which the objective is minimum are 1000 K and 1100–1750 K respectively. On (c), we see that the diffusion temperature corresponding to 3.25 nm large nanocavities, θ_{24}, is not clearly indicated by the *size* objective at 973 K, suggesting to search on the other temperatures.

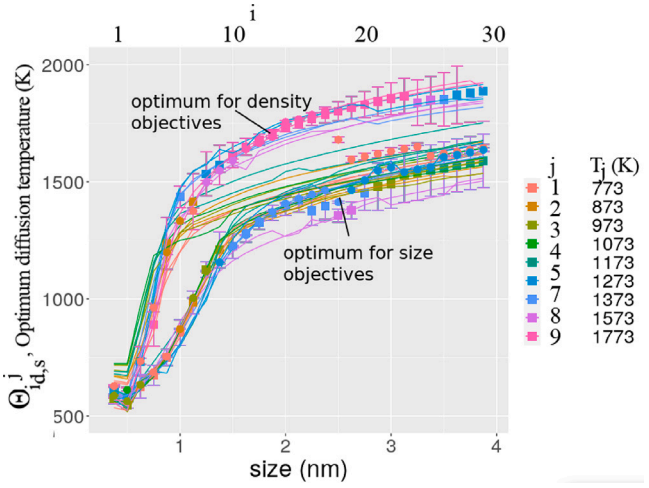

Fig. 7. Multi-objective optimization results shown in the parameter space. The lower x axis is the nanocavity size but the upper x axis is the parameter index i. Lines are $\Theta^j_{i\,d,s}$, the estimate of θ_i optimizing each $O^d(j)$ and each $O^s(j)$. Points are the *best* estimate values among j and the bars indicate the dispersion of the calculated points around the $\Theta^j_{i\,d,s}$.

Our results are compared to literature in Fig. 9 and do not differ significantly from what we obtained in [24] with a simplified approach. They agree with Mason's calculations of small vacancy clusters as well as with the classical surface diffusion model from [14] for large nanocavities. In Appendix G, this classical expression is given and adjusted on our results, which leads to an activation energy close to $E_s = 2.7 \pm 0.3$ eV. Finally, in the intermediate range of vacancy cluster sizes, we improve the weakly justified formula we proposed in [37] and Castin's calculations [17] which depend strongly on the quality of the empirical potential.

The other well known process that causes nanocavity growth is the dissociation of small cavities and the diffusion of the *released* vacancies toward larger cavities that thus grow. In this work, this process is not included in the OKMC model. As discussed in detailed in [24], we can define the *dissociation* temperatures as the temperature at which the probability of dissociation is one per second and then superpose them on the diffusion temperature in Fig. 9. In the conditions for which present nanocavities should dissociate, their diffusion is likely overestimated to compensate this missing process. It can happen where the green area is superposed to the rose area and. It is not observed for small nanocavities and it is comprised in the uncertainties on the diffusion temperature.

A detailed discussion on the experimental results can be found in [22] and on the limitation of our OKMC model in [25]. In this later paper, a significant part of the information to reproduce the results presented here can also be found: in particular, the model of the irradiation events and the parameters related to the presence of impurities. Note also that we are making efforts to give access to our databases as is done for the collision cascades https://cascadesdb.iaea.org and the point defect and the extended defect properties (https://db-amdis.org/defectdb).

The discussion remains open regarding a fully automatic optimization algorithm but the way we *manually* operated suggests that a genetic algorithm could be appropriate.

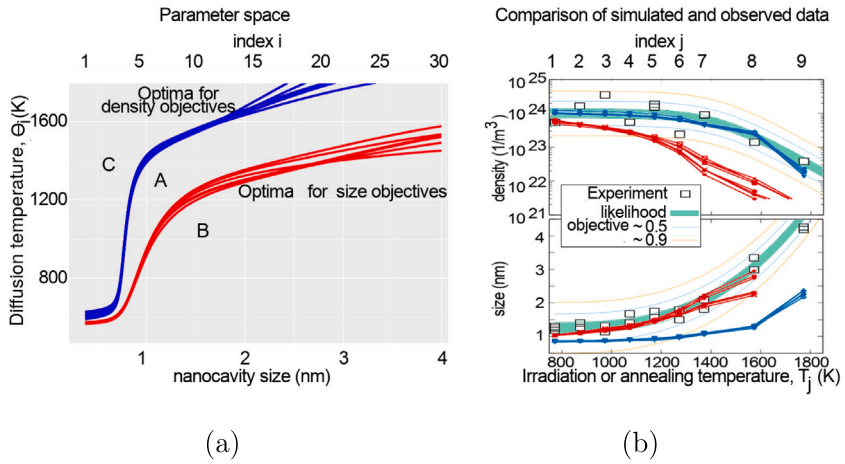

Fig. 8. (a) Example of optimum solutions of *density* objectives (blue) and *size* objectives (red) obtained as described in the text. (b) Comparison of the corresponding simulated *density* and *size* with the likelihood and the experimental points.

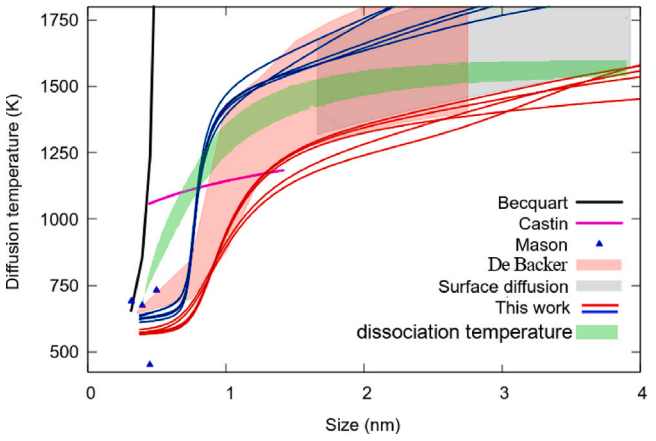

Fig. 9. Comparison of the good solutions of the Pareto front (red and blue) with Becquart [37], Castin [17], Mason [16] and De Backer [25]. It shows how, despite its uncertainties, our results improve the data on the nanocavity diffusion in tungsten. The grey area range of the classical surface diffusion model [14] is obtained with an effective activation energy of 2.40–3.05 eV in Eq. (G.1).

5. Conclusion

We combined experimental results of distributions of nanocavities formed in W at different temperatures with a multiscale model. To obtain the diffusion properties of nanocavities as a function of their size we had to develop a complex multi-objective optimization approach because the simple optimization methods failed. The representations of the results in a high dimensional space formed by the searched parameters and the objectives help to explore the set of all possibilities. The patterns observed on some projections on the coordinate planes indicated where to concentrate the search of the optimum solutions. The rewarding point of this multi-objective optimization is that on top of the estimation of the diffusion temperatures at which cavities of different sizes start moving, one has their uncertainty. The analysis of what causes the Pareto Front indicates how the uncertainties can be reduced and provide the processes/mechanisms missing in the model and help identifying the experimental conditions, not taken into account in our model, such as the formation of a small oxide layers on the sample surface which provide another source of vacancies.

CRediT authorship contribution statement

Andrée De Backer: Conceptualization, Data curation, Investigation, Methodology, Writing – original draft, Writing – review & editing. **Abdelkader Souidi:** Data curation, Investigation. **Etienne A. Hodille:** Data curation, Formal analysis, Visualization. **Emmanuel Autissier:** Data curation, Formal analysis. **Cécile Genevois:** Data curation, Formal analysis, Funding acquisition, Investigation, Methodology. **Farah Haddad:** Data curation, Formal analysis. **Antonin Della Noce:** Methodology, Writing – original draft, Writing – review & editing. **Christophe Domain:** Conceptualization, Data curation, Formal analysis, Software, Writing – original draft, Writing – review & editing. **Charlotte S. Becquart:** Conceptualization, Formal analysis, Funding acquisition, Methodology, Writing – original draft, Writing – review & editing. **Marie France Barthe:** Data curation, Formal analysis, Funding acquisition, Supervision, Validation.

Declaration of competing interest

The authors declare that they have no known competing financial interests or personal relationships that could have appeared to influence the work reported in this paper.

Acknowledgments

This work has been carried out within the framework of the EUROfusion Consortium and has received funding from the Euratom research and training programme 2014–2018 and 2019–2020 under grant agreement No 633053. The views and opinions expressed herein do not necessarily reflect those of the European Commission. The project leading to this publication has received funding from Excellence Initiative of Aix-Marseille University - A*MIDEX, a French Investissements d'Avenir programme as well as from the French National Research Agency (Grant No. ANR-18-CE05-0012). Centre de Calcul Intensif d'Aix-Marseille is acknowledged for granting access to its high performance computing resources. Images and some analysis have been obtained using OVITO [38].

Appendix A. Model inputs

Three main categories of the OKMC model inputs:

- The simulation box properties are given by the box size, temperature, time and box boundary conditions.

(a)

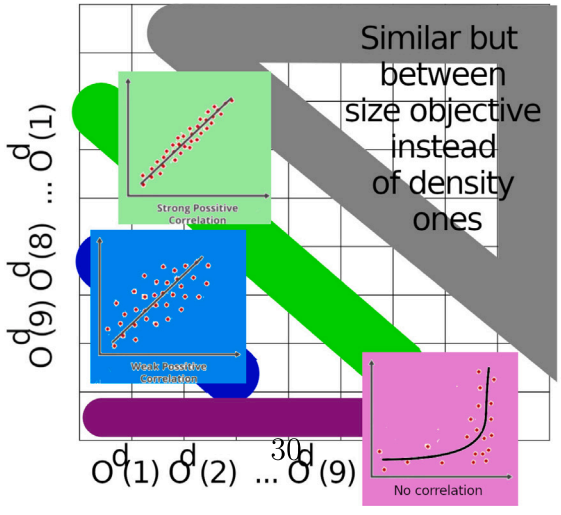

(b)

Fig. D.10. (a) Facet plot (figures made up of multiple subplots which have the similar set of axes) represented as a square matrix where each subplot shows the correlation between (O^j_d and O^k_d) thanks to the data on (O^j_d, O^k_d) planes, below the diagonal (resp. (O^j_s, O^k_s) above the diagonal). (b) Schematic drawing of the qualitative correlations observed in the subplots: near the diagonal, points tend to be correlated.

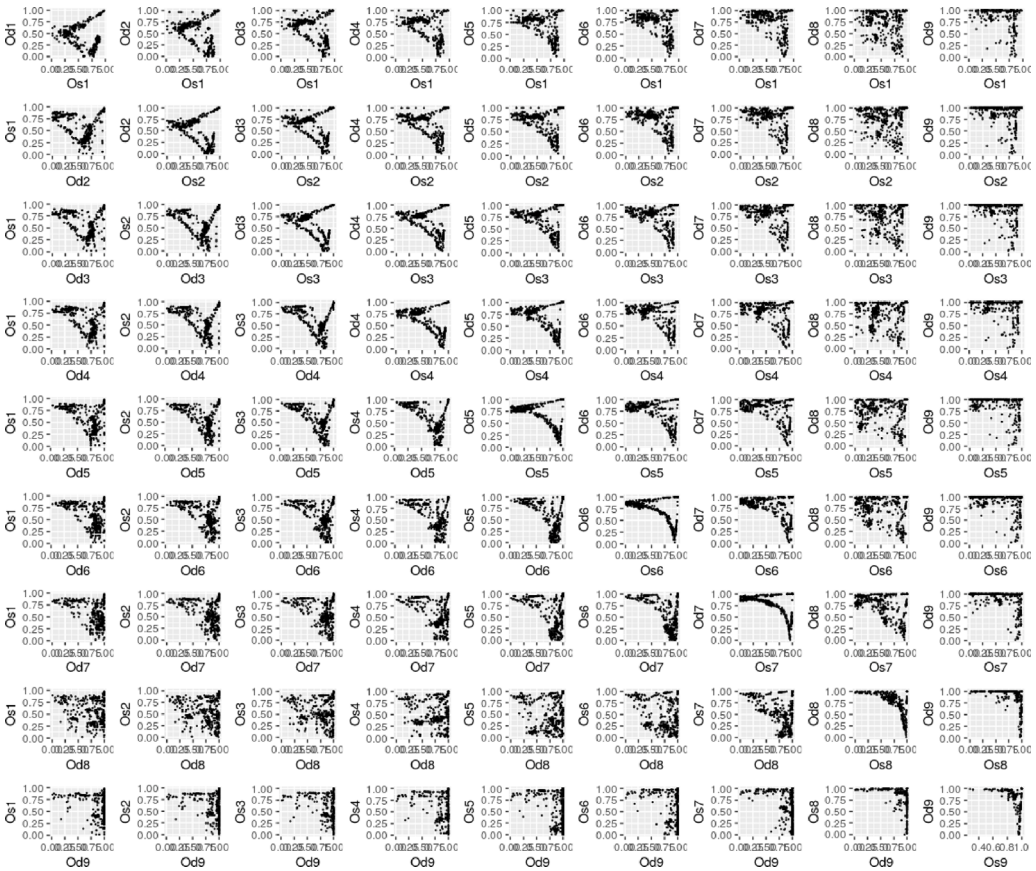

Fig. D.11. Facet plots (figures made up of multiple subplots which have the similar set of axes) represented as a square matrix where each subplot shows the correlation between (O_d^j and O_s^k) thanks to the projection of the data in (O_d^j, O_s^k) planes.

- The defect source, the irradiation, is simulated by introduction of cascade debris. They are obtained combining several cascade databases. Our method reproduces the damage flux, the defect clustering and spatial distribution of the primary damage.
- The defect diffusion and dissociation are given by Arrhenius formulae and the defect interactions are controlled by pre-defined capture distances.
- The materials impurities are taken into account with a list of traps whose properties are based on a large database of Density Functional Theory calculations. Impurities can strongly impact the microstructure evolution even when they are in small concentration.

Appendix B. Attempt frequency of the nanocavities diffusion

The attempt frequency is defined on 3 domains:

$$f(s) = \begin{cases} f^0 & s < 0.55 \text{ nm} \\ \text{interpolation} & 0.55 \text{ nm} \le s < 0.95 \text{ nm} \\ \frac{f^1}{s^4} & 0.95 \text{ nm} \le s \end{cases} \tag{B.1}$$

where $f^0 = 6.5 \times 10^{12}$ s^{-1} is a value near Debye frequency usually taken for small defects. For large nanocavities, the frequency is defined as the ratio of f^1 divided by s^{-4} as justified by the classical theory of surface diffusion [14]. The small and large size range are smoothly connected with (also described in [25])

$$f(s) = f^1 \left(\exp\left(-\frac{n(s)}{n^{cav}}\right) + 7\left(\frac{4\pi}{3n(s)}\right)^{\frac{4}{3}} \left(1 - \exp\left(-\frac{n(s)}{n^{cav}}\right)\right)^2 \right) \tag{B.2}$$

with $n^{cav} = 28$, f^1 a parameter equal to 6.5×10^{12} s^{-1} as for n equal 1 to 5 and where the relation between n, the number of defects and s, the defect size (diameter) is $n(s) = \frac{\pi}{3}\left(\frac{s}{a}\right)^3$.

Appendix C. Likelihood on experimental data

The likelihood is a 4 parameters function adjusted on experimental data equal to

$$\begin{aligned} density_{obs}(T) &= p_0^d + \frac{p_1^d}{1+\exp\left(\frac{T-p_2^d}{p_3^d}\right)} \\ size_{obs}(T) &= p_0^s + \frac{p_1^s}{1+\left(\frac{T-p_2^s}{p_3^s}\right)} \end{aligned} \tag{C.1}$$

with the parameters $p^d = [0, 10^{24}, 1428, 105]$ and $p^s = [1.26, 773, 643, 2.8]$.

Appendix D. Illustrations of other projections

In our work, each simulation is considered as a point described by N components in the parameter space and $2M$ components in the objective space, hence $30+2\times9 = 48$. In Section 3.1, we described some of the projections of our data on planes defined by pairs of objectives (O_d^j, O_s^j) of same index. There are nine such planes. In principle, all planes can be considered, i.e. $M(M-1) = 153$. These projections are illustrated by thumbnails in Figs. D.10 and D.11. The interdependence of objective i to objective $i-1$ can be seen as well as the persistence of the 3 branch structures in (O_d^j, O_s^k) projections.

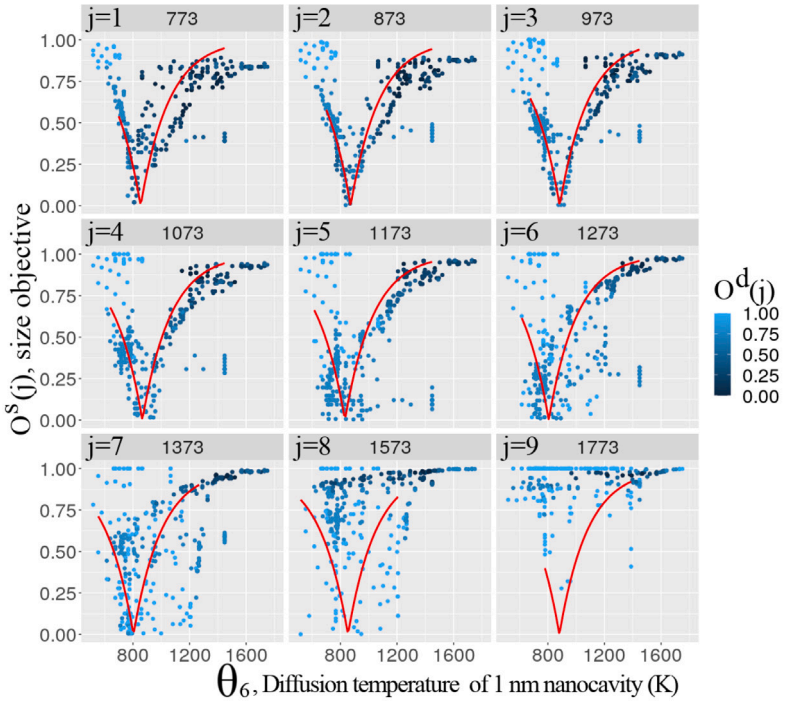

(a)

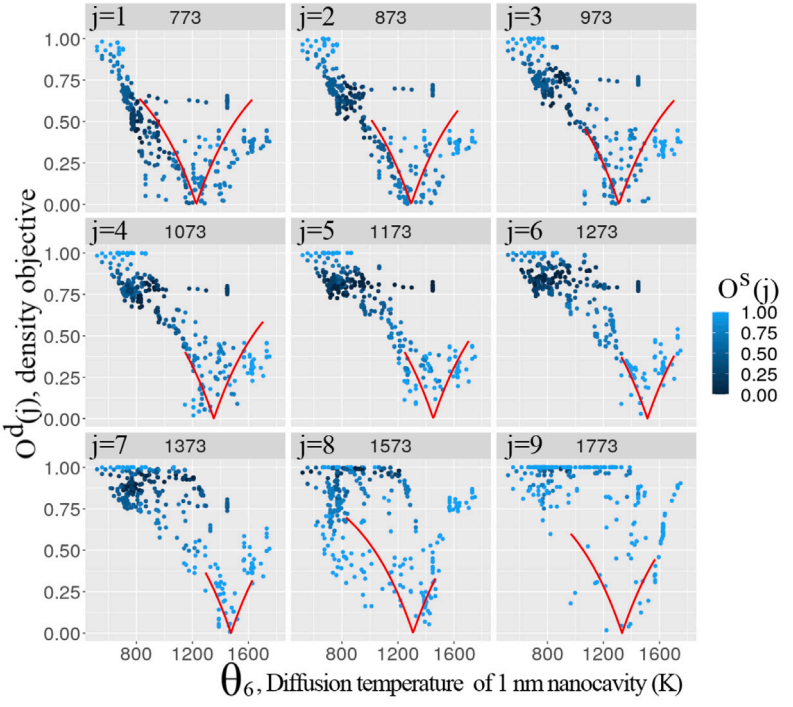

(b)

Fig. D.12. (a) Size objectives for all j as a function of θ_6 and (b) density objectives for all j as a function of θ_6. Red curves are the fits using Eq. (E.1) to obtain the optimum $\Theta^j_{i_d,s}$ in each condition.

Table F.1
Set of parameters for Eq. (F.1) used for Fig. 8. The type is *d* for the *density* side of the Pareto front and *s* for the *size* side of the Pareto front.

p_1	p_2	p_3	p_4	p_5	Type
618	226	100.0	0.628	0.127	d
548	296	88.6	0.687	0.146	d
515	301	74.3	0.643	0.176	d
503	296	83.6	0.664	0.211	d
499	326	73.7	0.726	0.240	d
533	243	60.6	0.931	0.288	s
540	276	40.6	0.931	0.409	s
548	259	46.3	1.020	0.397	s
533	277	22.5	0.957	0.459	s
524	191	109.0	0.826	0.319	s

Appendix E. Fit of objectives

The two parameter (A, xmin) expression fitted on each objective as a function of each θ_i is

$$y(x) = 1 - exp(-A|x - xmin|). \tag{E.1}$$

The results for θ_6 are illustrated in Fig. D.12.

Appendix F. Parametric function for the diffusion temperature

The diffusion temperatures shown in Fig. 8 are given by

$$\begin{aligned}\theta(s) = \quad & p_1 + p_2 \left(1 + \tfrac{2}{\pi}\text{atan}(\tfrac{s-p_4}{p_5})\right)^2 \\ & + p_3 \left(1 + \tfrac{2}{\pi}\text{atan}(\tfrac{s-1.5}{2})\right)^2\end{aligned} \tag{F.1}$$

which has 3 parameters of temperature unit, p_1, p_2 and p_3, 2 parameters of length unit, p_4 and p_5 and uses the arc tangent to make a smooth transition. Parameters are given in Table F.1.

Appendix G. Surface diffusion coefficient

In [14] for large nanocavities, the surface diffusion expression is

$$D(r) = \frac{9\Omega^{4/3} D_s}{\pi^3 r_n^4} \text{ with } D_s = \frac{\alpha_s^2}{4} \exp\left(-\frac{E_s}{k_B T}\right) \tag{G.1}$$

where Ω is the atomic volume, r is here the radius, D_s is the surface diffusion coefficient expressed by an Arrhenius law with α_s, the surface jump distance and E_s is the activation energy of the surface diffusion. In this expression, the most important parameter is the activation energy and there is no direct way to calculate it. Adjusting the formula on our results, we obtain $E_s = 2.40$–3.05 eV.

Data availability

An example of the OKMC input and the raw data to reproduce the graphs of this articles will be available at https://data.mendeley.com/my-data/; further inquiries can be directed to the corresponding author.

References

[1] M. Oya, M. Shimada, C. Taylor, M. Kobayashi, Y. Nobuta, Y. Yamauchi, Y. Oya, Y. Ueda, Y. Hatano, Deuterium retention in tungsten irradiated by high-dose neutrons at high temperature, Nucl. Mater. Energy 27 (2021) 100980, http://dx.doi.org/10.1016/j.nme.2021.100980.

[2] M. Rieth, R. Doerner, A. Hasegawa, Y. Ueda, M. Wirtz, Behavior of tungsten under irradiation and plasma interaction, J. Nucl. Mater. 519 (2019) 334–368, http://dx.doi.org/10.1016/j.jnucmat.2019.03.035.

[3] C. Domain, C.S. Becquart, Object kinetic Monte Carlo (OKMC): A coarse-grained approach to radiation damage, in: W. Andreoni, S. Yip (Eds.), Handbook of Materials Modeling : Methods: Theory and Modeling, Springer International Publishing, 2018, pp. 1–26, http://dx.doi.org/10.1007/978-3-319-42913-7_101-1.

[4] M.J. Caturla, Object kinetic Monte Carlo methods applied to modeling radiation effects in materials, Comput. Mater. Sci. 156 (2019) 452–459, http://dx.doi.org/10.1016/j.commatsci.2018.05.024.

[5] P. Benoist, G. Martin, Stability of Void Lattice Under Irradiation: A Kinetic Model, USEDA Report CONF-751006-P2, Vol. 2, 1976, p. 1236.

[6] K. Krishan, Kinetics of void-lattice formation in metals, Nature 287 (1980) 420, http://dx.doi.org/10.1038/287420a0.

[7] J. Marian, V.V. Bulatov, Stochastic cluster dynamics method for simulations of multispecies irradiation damage accumulation, J. Nucl. Mater. 415 (1) (2011) 84–95, http://dx.doi.org/10.1016/j.jnucmat.2011.05.045.

[8] T. Jourdan, J.-P. Crocombette, Rate theory cluster dynamics simulations including spatial correlations within displacement cascades, Phys. Rev. B 86 (2012) 054113, http://dx.doi.org/10.1103/PhysRevB.86.054113.

[9] T. Jourdan, Influence of dislocation and dislocation loop biases on microstructures simulated by rate equation cluster dynamics, J. Nucl. Mater. 467 (2015) 286–301, http://dx.doi.org/10.1016/j.jnucmat.2015.09.046.

[10] Y. Li, S. Hu, X. Sun, M. Stan, A review: applications of the phase field method in predicting microstructure and property evolution of irradiated nuclear materials, npj Comput. Mater. 3 (2017) 16.

[11] S. Hu, C. Henager, Phase-field simulation of void migration in a temperature gradient, Acta Mater. 58 (2010) 3230, http://dx.doi.org/10.1016/j.actamat.2010.01.043.

[12] S. Benannoune, Y. Charles, J. Mougenot, M. Gaspérini, G.D. Temmerman, Multidimensional finite-element simulations of the diffusion and trapping of hydrogen in plasma-facing components including thermal expansion, Phys. Scr. 2020 (T171) (2020) 014011, http://dx.doi.org/10.1088/1402-4896/ab4335.

[13] F. Nichols, Kinetics of diffusional motion of pores in solids: A review, J. Nucl. Mater. 30 (1) (1969) 143–165.

[14] P.J. Goodhew, S.K. Tyler, Helium bubble behaviour in b. c. c. metals below 0.65Tm, Proc. R. Soc. Lond. A 377151–184 (1981).

[15] V. Zell, H. Trinkaus, H. Schroeder, A simulation study of the migration and coalescence of gas bubbles in metals, J. Nucl. Mater. 212–215 (1994) 320–324.

[16] D.R. Mason, D. Nguyen-Manh, C.S. Becquart, An empirical potential for simulating vacancy clusters in tungsten, J. Phys.: Condens. Matter. 29 (50) (2017) 505501.

[17] N. Castin, A. Bakaev, G. Bonny, A. Sand, L. Malerba, D. Terentyev, On the onset of void swelling in pure tungsten under neutron irradiation: An object kinetic Monte Carlo approach, J. Nucl. Mater. 493 (2017) 280–293.

[18] D. Perez, L. Sandoval, S. Blondel, B.D. Wirth, B.P. Uberuaga, A.F. Voter, The mobility of small vacancy/helium complexes in tungsten and its impact on retention in fusion-relevant conditions, Sci. Rep. 7 (1) (2017) 2522.

[19] V. Jansson, M. Chiapetto, L. Malerba, The nanostructure evolution in Fe–C systems under irradiation at 560K, J. Nucl. Mater. 442 (1) (2013) 341–349.

[20] B. Pannier, Towards the Prediction of Microstructure Evolution Under Irradiation of Model Ferritic Alloys with an Hybrid AKMC-OKMC Approach (Ph.D. thesis), University of Lille 1, 2017, URL http://www.theses.fr/2017LIL10061.

[21] J. Hou, Y.-W. You, X.-S. Kong, J. Song, C. Liu, Accurate prediction of vacancy cluster structures and energetics in bcc transition metals, Acta Mater. 211 (2021) 116860, http://dx.doi.org/10.1016/j.actamat.2021.116860.

[22] E. Autissier, F. Farah, C.G. Mazellier, B. Decamps, R. Schäublin, M.F. Barthe, Cavity evolution as a function of temperature in self irradiated tungsten, 2025, in preparation.

[23] A. Chauhan, Q. Yuan, D. Litvinov, E. Gaganidze, H.-C. Schneider, D. Terentyev, J. Aktaa, Effect of temperature on the neutron irradiation-induced cavities in tungsten, Phil. Mag. 102 (2022) 1665–1683, http://dx.doi.org/10.1080/14786435.2022.2079750.

[24] A. De Backer, A. Souidi, E.A. Hodille, E. Autissier, C. Genevois, F. Haddad, A. Della Noce, C. Domain, C.S. Becquart, M.F. Barthe, Multi-objective optimization of the nanocavities diffusion in irradiated metals, Phys. Sci. Forum 5 (1) (2022) http://dx.doi.org/10.3390/psf2022005041.

[25] A. De Backer, A. Souidi, E.A. Hodille, E. Autissier, C. Genevois, F. Haddad, A. Della Noce, C. Domain, C.S. Becquart, M.-F. Barthe, Readdressing nanocavity diffusion in tungsten, Front. Nucl. Eng. 2 (2023) 1240995, http://dx.doi.org/10.3389/fnuen.2023.1240995.

[26] C.S. Becquart, A. De Backer, C. Domain, Atomistic modeling of radiation damage in metallic alloys, in: S. Schmauder, C.-S. Chen, K.K. Chawla, N. Chawla, W. Chen, Y. Kagawa (Eds.), Handbook of Mechanics of Materials, Springer Singapore, Singapore, 2019, pp. 673–701.

[27] A. Fedorov, Evolution of Point Defect Clusters During Irradiation and Thermal Treatment (An Ion Implantation and Thermal Desorption Study) (Ph.D. thesis), University of Delf.

[28] J. Boisse, D.B. Andree, C. Domain, C. Becquart, Modeling of the self trapping of helium and the trap mutation in tungsten using DFT and empirical potentials based on DFT, J. Mater. Res. 29 (2014) 2374–2386.

[29] A. Drexler, L. Vandewalle, T. Depover, K. Verbeken, J. Domitner, Critical verification of the Kissinger theory to evaluate thermal desorption spectra, Int. J. Hydrog. Energy 46 (79) (2021) 39590–39606.

[30] G.E.P. Box, G.C. Tiao, Bayesian Inference in Statistical Analysis, Addison-Wesley Pub. Co., Reading, Mass, 1973.

[31] D.B. Nelson, Conditional heteroskedasticity in asset returns: A new approach, Econometrica 59 (2) (1991) 347–370.
[32] S. Hasanzadeh, R. Schäublin, B. Décamps, V. Rousson, E. Autissier, M.F. Barthe, C. Hébert, Three-dimensional scanning transmission electron microscopy of dislocation loops in tungsten, Micron 113 (2018) 24–33.
[33] Z. Hu, P. Desgardin, C. Genevois, J. Joseph, B. Décamps, R. Schäublin, M.-F. Barthe, Effect of purity on the vacancy defects induced in self–irradiated tungsten: A combination of PAS and TEM, J. Nucl. Mater. 556 (2021) 153175.
[34] D.T. Gillespie, A general method for numerically simulating the stochastic time evolution of coupled chemical reactions, J. Comput. Phys. 22 (1976) 403.
[35] L.T. Kong, L.J. Lewis, Transition state theory of the preexponential factors for self-diffusion on Cu, Ag, and Ni surfaces, Phys. Rev. B 74 (2006) 073412.
[36] C. Lin, H. Ruan, S.-Q. Shi, Mechanical–chemical coupling phase-field modeling for inhomogeneous oxidation of zirconium induced by stress–oxidation interaction, npj Mater Degrad 4 (2020) 22.
[37] C. Becquart, C. Domain, U. Sarkar, A. De Backer, M. Hou, Microstructural evolution of irradiated tungsten: Ab initio parameterisation of an OKMC model, J. Nucl. Mater. 403 (1) (2010) 75–88.
[38] A. Stukowski, Visualization and analysis of atomistic simulation data with OVITO–the open visualization tool, Modelling Simul. Mater. Sci. Eng. 18 (1) (2009) 015012.